Electrochemical and Structural Investigation of Calcium Substituted Monoclinic $Li_3V_2(PO_4)_3$ Anode Materials for Li-Ion Batteries

*Qiang Fu, Shuoqi Liu, Angelina Sarapulova, Lihua Zhu, Martin Etter, Edmund Welter, Peter G. Weidler, Michael Knapp, Helmut Ehrenberg, and Sonia Dsoke**

In this work, the effect of Li^+ substitution in $Li_3V_2(PO_4)_3$ with a large divalent ion (Ca^{2+}) toward lithium insertion is studied. A series of materials, with formula $Li_{3-2x}Ca_xV_2(PO_4)_3$/C (x = 0, 0.5, 1, and 1.5) is synthesized and studied in the potential region 3–0.01 V versus Li^+/Li. Synchrotron diffraction demonstrates that $Li_3V_2(PO_4)_3$/C has a monoclinic structure (space group $P2_1/n$), while $Ca_{1.5}V_2(PO_4)_3$/C possesses a rhombohedral structure (space group R-3c). The intermediate compounds, $Li_2Ca_{0.5}V_2(PO_4)_3$/C and $LiCaV_2(PO_4)_3$/C, are composed of two main phases, including monoclinic $Li_3V_2(PO_4)_3$/C and rhombohedral $Ca_{1.5}V_2(PO_4)_3$/C. Cyclic voltammetry reveals five reduction and oxidation peaks on $Li_3V_2(PO_4)_3$/C and $Li_2Ca_{0.5}V_2(PO_4)_3$/C electrodes. In contrast, $LiCaV_2(PO_4)_3$/C and $Ca_{1.5}V_2(PO_4)_3$/C have no obvious oxidation and reduction peaks but a box-type voltammogram. This feature is the signature for capacitive-like mechanism, which involves fast electron transfer on the surface of the electrode. $Li_3V_2(PO_4)_3$/C undergoes two solid-solution and a short two-phase reaction during lithiation and delithiation processes, whereas $Ca_{1.5}V_2(PO_4)_3$/C only goes through capacitive-like mechanism. In operando X-ray absorption spectroscopy confirms that, in both $Li_3V_2(PO_4)_3$/C and $Ca_{1.5}V_2(PO_4)_3$/C, V ions are reduced during the insertion of the first three Li ions. This study demonstrates that the electrochemical characteristic of polyanionic phosphates can be easily tuned by replacing Li^+ with larger divalent cations.

1. Introduction

Nowadays, lithium-ion batteries (LIBs) play a very important role in our daily life and society. Indeed, LIBs are widely used in portable electrical devices, such as mobile phones, laptops, and digital electronics.[1] However, improvement is still required to make this technology also suitable for the large-scale grid, hybrid electric vehicles (HEV), plug-in hybrid electric vehicles (PHEV), and pure electric vehicles (PEV), where high energy density is on demand. In order to further increase the energy density, it is urgent to develop positive electrode materials with high potential and high capacity and negative electrode materials with high capacity.[2] In addition, the materials should deliver high power and good cycling stability.

Thanks to its high operating potential, high thermal stability, and low synthetic costs, lithium vanadium phosphate, $Li_3V_2(PO_4)_3$ (LVP), has recently attracted much attention as a cathode material for lithium-ion batteries.[2b,3] Its high power ability (due to its high diffusion coefficient) and exceptional stability make this material very attractive also in hybrid supercapacitor devices.[4] LVP has two different crystal structures:[5] the rhombohedral structure, with the space group R-3 and the monoclinic one, with the space group $P2_1/n$.

The rhombohedral LVP (NASICON-type) consists of $[VO_6]$ octahedra and $[PO_4]$ tetrahedra connected through shared corners, forming $[V_2(PO_4)_3]$ "lantern" units, stacked along the [001] direction, where lithium ions lie to a unique 4-fold coordinated crystallographic site. Due to the

Dr. Q. Fu, S. Liu, Dr. A. Sarapulova, L. Zhu, Dr. M. Knapp, Prof. H. Ehrenberg, Dr. S. Dsoke
Institute for Applied Materials (IAM)
Karlsruhe Institute of Technology (KIT)
Hermann-von-Helmholtz-Platz 1
D-76344 Eggenstein-Leopoldshafen, Germany
E-mail: sonia.dsoke@kit.edu

The ORCID identification number(s) for the author(s) of this article can be found under https://doi.org/10.1002/aenm.201901864.

DOI: 10.1002/aenm.201901864

Dr. M. Etter, Dr. E. Welter
Deutsches Elektronen-Synchrotron DESY
Notkestraße 85, D-22607 Hamburg, Germany

Dr. P. G. Weidler
Institute of Functional Interfaces (IFG)
Chemistry of Oxidic and Organic Interfaces (COOI)
Karlsruhe Institute of Technology (KIT)
Hermann-von-Helmholtz-Platz 1
D-76344 Eggenstein-Leopoldshafen, Germany

Dr. M. Knapp, Prof. H. Ehrenberg, Dr. S. Dsoke
Helmholtz Institute Ulm for Electrochemical Energy Storage (HIU)
Helmholtzstrasse 11, 89081 Ulm, Germany

variety of oxidation states of vanadium and its open structure, LVP can be used in a wide potential range and it can be, therefore, employed as both cathode and anode in a Li-ion battery. As a cathode material, rhombohedral LVP[5a] exhibits a very flat plateau at around 3.75 V versus Li^+/Li. This plateau corresponds to a two-phase transition between the compositions $Li_3V_2(PO_4)_3$ and $Li_1V_2(PO_4)_3$. In contrast, when used as negative electrode in the potential range of 3.0–1.0 V versus Li^+/Li, the rhombohedral LVP shows a short slope and a plateau at around 1.75 V related to the V^{3+}/V^{2+} redox couple. As proved by Jian et al. through in operando XRD, it underwent a solid-solution reaction during Li insertion in rhombohedral LVP.[6]

On the other hand, monoclinic LVP has a 3D network consisting of slightly distorted $[VO_6]$ octahedra and $[PO_4]$ tetrahedra linked together via sharing oxygen vertexes, where lithium atoms occupy three distinct crystallographic positions (Figure S1, Supporting Information). Li(1) lies at the tetrahedral site, while Li(2) and Li(3) are located in two pseudotetrahedral sites, as proved by ^{7}Li NMR spectrum.[7] Compared with rhombohedral LVP, monoclinic LVP shows enhanced electrochemical properties due to the higher mobility of all three Li.[2b] Thus, many researchers have focused on the monoclinic phase as cathode material. However, the pure LVP suffers from low intrinsic electronic conductivity,[7,8] which may limit the application of this material in high power devices, like Li-ion capacitors.

The problem of low electronic conductivity can be overcome by two strategies: surface carbon coating or substitution of Li or V in some degree with other metals. The first strategy has also the additional benefit that carbon plays a reducing agent role to reduce V^{5+} to V^{3+} during the synthesis.[9] Moreover, in situ carbon coating could relieve the growing up and aggregation of LVP/C particles during annealing at high temperature.[10] On the other hand, great efforts have been devoted in the last years to the second strategy. Li^+ extraction/insertion and the electronic conductivity can be effectively improved by substituting V^{3+} with other metal ions, such as Mg^{2+}, Co^{2+}, Fe^{3+}, Ni^{2+}, etc., resulting in improved cycling stability and rate capability.[4,9,11] Additionally, heterovalent substitution could provide vacancies,[12] which can help to accommodate more Li ions, thus providing a higher capacity when LVP is used as negative electrode.

Recently, the substitution of metal cations at the Li sites, instead of the V sites, in the LVP/C system, was also investigated. For example, Yin et al.[13] prepared Mg^{2+}-doped $Li_{3-2x}Mg_xV_2(PO_4)_3/C$ by sol–gel method and investigated it as cathode material for Li-ion batteries. They found that a small amount of Mg^{2+} at Li sites does not significantly change the crystal structure of $Li_3V_2(PO_4)_3/C$. In addition, Mg-doped $Li_3V_2(PO_4)_3/C$ has larger cell volume than the pristine $Li_3V_2(PO_4)_3/C$, which can facilitate the Li^+ transport into the structure. Furthermore, low content Ca-substituted LVP with formula of $Li_{2.96}Ca_{0.02}V_2(PO_4)_3$ was prepared via a hydrothermal method by Goodenough et al.[14] and used as cathode material, which shows improved capacity retention at high rates. However, the influence of the divalent ion substitution is evaluated only in the high potential region (3–4.3/4.8 V vs Li^+/Li). So far, no reports describe if the substitution of Li^+ with a M^{2+} can affect the electrochemistry in the low potential region (3.0–0.01 V vs Li^+/Li). Only few studies have been reported on the use of LVP (and its derivatives) in the extended potential range 3.0–0.01 V versus Li^+/Li.[15] In this potential range, the LVP/C material displays a stable reversible capacity of 203 mAh g^{-1} at low current,[15a] an acceptable value but which is still lower than the one of graphite. Zhang et al.[15b] reported a nanostructured carbon coated LVP with outstanding rate capability, when used as negative electrode, with a high capacity of 100 mAh g^{-1} at 100C. The in operando XRD[15b] reveals the two-phase reaction in the potential range 3–1.5 V (insertion of 2 Li^+) followed by a solid solution process in the region 1.5–0 V (insertion of additional 2 Li^+). However, though in the low potential region the V^{2+}/V^+ redox couple was proposed,[15a] there is no detailed work to prove the change in oxidation state of vanadium and the local electronic structure of LVP.

On the basis of these considerations, in this work we aim to understand the effect of Li^+ substitution in LVP with a divalent metal (Ca^{2+} in this case from low to high contents) in the potential region 3–0.01 V versus Li^+/Li. In this purpose, we prepared a series of materials with formula $Li_{3-2x}Ca_xV_2(PO_4)_3/C$ (x = 0, 0.5, 1, and 1.5). The working mechanism of pure LVP and $Ca_{1.5}V_2(PO_4)_3/C$ was elucidated by in operando synchrotron diffraction and in operando X-ray absorption spectroscopy (XAS), very powerful tools to probe the structural evolution and electronic structure and oxidation state changes during lithiation and delithiation. From the electrochemical performance point of view, the replacement of Li^+ with Ca^{2+} in $Li_3V_2(PO_4)_3/C$ confers good rate performance and enhanced capacity. Here it is the first time observed that the quantity of Ca can drastically change the electrochemical signature of these materials. Therefore, this kind of material is a promising candidate for the realization of advanced high power and energy devices.

2. Results and Discussion

2.1. Structural and Morphological Characterization

To determine the carbon content in $Li_{3-2x}Ca_xV_2(PO_4)_3/C$, thermogravimetric analysis (TGA) was performed by heating the samples under O_2 flow. As shown in Figure S2a (Supporting Information), the weight loss before 380 °C is attributed to the evaporation of absorbed and chemically bonded water in the sample, while the abrupt weight loss between 380 and 550 °C is attributed to the combustion of residual carbon.[16] The carbon content in $Li_{3-2x}Ca_xV_2(PO_4)_3/C$ materials is estimated to be 8.06, 5.47, 6.03, and 3.89 wt%, respectively, when x = 0, 0.5, 1.0, and 1.5.

Argon gas sorption isotherms were used to probe the Brunauer–Emmett–Teller (BET) surface area and the porous structure of all samples (Figure S2b, Supporting Information). The BET surface area of LVP/C is 54.3 m^2 g^{-1}, while the one of $Ca_{1.5}VP/C$ is only 24.8 m^2 g^{-1}. The two intermediate compositions $Li_2Ca_{0.5}V_2(PO_4)_3/C$ and $LiCaV_2(PO_4)_3/C$ have BET surface area of 32.6 and 39.8 m^2 g^{-1}, respectively. The pore-size distribution curves show that the pore size for all samples lies in both, the micro- and mesopore range. In the case of LVP/C, the micro- and mesopores contribute about 90% to the total pore volume (which is calculated at a p/p_o of 0.99). In the case of the other three samples this value is the same and lay at about 60%. These meso- and micropores in all materials could be beneficial

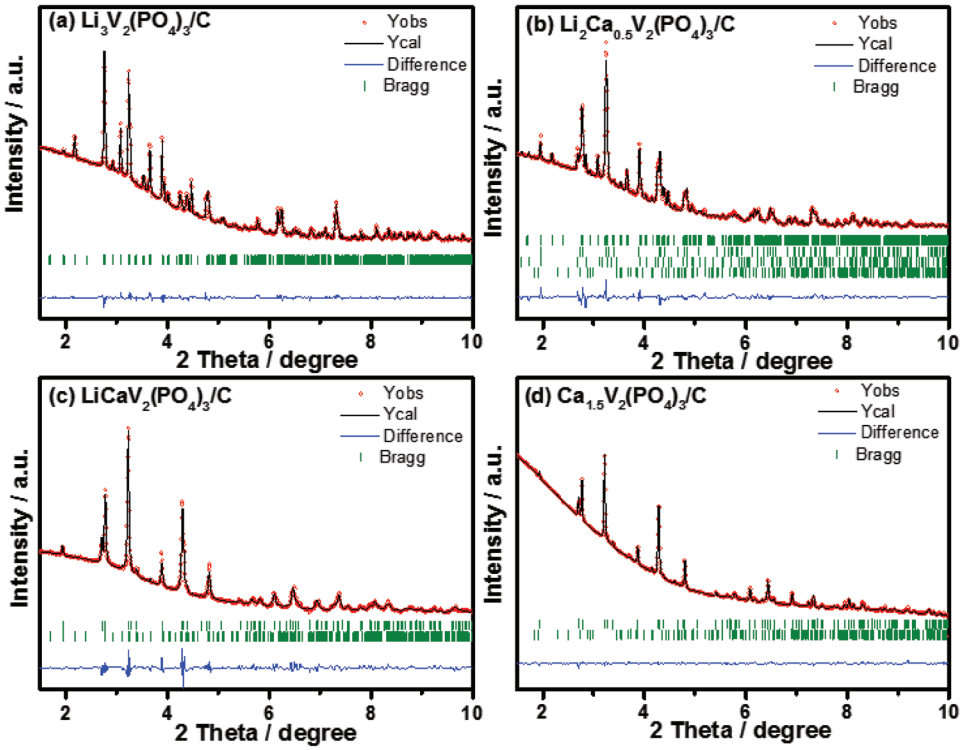

Figure 1. Rietveld refinement of the synchrotron diffraction patterns of the $Li_{3-2x}Ca_xV_2(PO_4)_3$/C.

to the electrochemical performance because of the shorter diffusion distance and low ion-transport resistance as well as good access of electrolyte to the electrode surface.[17]

The crystal structure of the as-prepared samples was characterized by synchrotron diffraction, as displayed in **Figure 1**. All featured diffraction reflections observed for the pristine $Li_3V_2(PO_4)_3$/C can be well indexed to the monoclinic phase $Li_3V_2(PO_4)_3$ with the space group of $P2_1/n$, which is in good agreement with a previous report.[5b] On the other hand, there is no evidence of diffraction reflections related to the carbon, suggesting that the residual carbon is amorphous and its presence does not affect the structure of LVP/C. The fully substituted material $Li_{3-2x}Ca_xV_2(PO_4)_3$/C (x = 1.5) has a rhombohedral structure with the space group R-3c, including a 5 wt% of $Ca_3(PO_4)_2$ as an impurity, as determined via Rietveld refinement. The two intermediate compositions $Li_2Ca_{0.5}V_2(PO_4)_3$/C and $LiCaV_2(PO_4)_3$/C are mixtures of monoclinic phase $Li_3V_2(PO_4)_3$ and rhombohedral structure $Ca_{1.5}V_2(PO_4)_3$ with the formation of solid solutions. The structural and the lattice parameters related to the main phase $Li_{3-2x}Ca_xV_2(PO_4)_3$/C (x = 0.0, 0.5, 1.0, 1.5) are given in Table S1 (Supporting Information). $Li_2Ca_{0.5}V_2(PO_4)_3$/C is composed of more phases: a main phase solid-solution on the base of monoclinic $Li_3V_2(PO_4)_3$ with a space group of $P2_1/n$ (45%) and a solid-solution on the base of rhombohedral $Ca_{1.5}V_2(PO_4)_3$ with a space group of R-3c (35%), a 18% of rhombohedral $Ca_{1.5}V_2(PO_4)_3$ with space group of R-3 and finally a 2% of $Ca_3(PO_4)_2$ as impurity. On the other side, the $LiCaV_2(PO_4)_3$/C can be identified as a mixture of two phases, including a solid-solution monoclinic $Li_3V_2(PO_4)_3$ with a space group of $P2_1/n$ and a solid-solution rhombohedral $Ca_{1.5}V_2(PO_4)_3$/C with a space group of R-3c. According to Vegard's law,[18] the lattice parameters of the mixture with x = 0.5 and 1 are different to the last one of boundary compounds. Similarly, other electrode materials with solid-solution behavior, obtained via substitution, have been reported. For example, Qing et al.[19] reported nanosized $LiNi_xFe_{1-x}PO_4$ solid solution prepared via a solid-state reaction method. $LiNi_xFe_{1-x}PO_4$ shows a single phase olivine-type structure with *Pnma* space group. Lattice parameters and chemical composition of the $LiNi_xFe_{1-x}PO_4$ follows the Vegard's law.[18] In our case, the lattice parameters of LVP/C are a = 8.6117 Å, b = 8.6004 Å, c = 12.0437 Å, and β = 90.5365°, while the lattice parameters of the compound with the main phase based on x = 1.5 ($Ca_{1.5}V_2(PO_4)_3$/C, 95%, impurity $Ca_3(PO_4)_2$) are $a = b$ = 8.5759 Å and c = 21.7765 Å. $Li_2Ca_{0.5}V_2(PO_4)_3$/C consists of 93.5% LVP/C and 6.5% $Ca_{1.5}V_2(PO_4)_3$/C. A decrease of a, b, and β and an increase of c, related to monoclinic phase, can be observed along with the increase of Ca substitution into LVP. On the other hand, the decrease of a and c is observed along with the Li substitution into $Ca_{1.5}V_2(PO_4)_3$. The larger cell volume of $Ca_{1.5}V_2(PO_4)_3$ could provide wider channels for Li^+ transport and facilitate the diffusion of Li^+ in the active materials, which can be beneficial for improving the electrochemical performance of $Li_{3-2x}Ca_xV_2(PO_4)_3$/C.

Scanning electron microscopy (SEM) shows that all the $Li_{3-2x}Ca_xV_2(PO_4)_3$/C samples are composed of submicron particles with agglomerated of about 100–600 nm, as shown in Figure S3 (Supporting Information). Besides, $Li_3V_2(PO_4)_3$/C and $Li_2Ca_{0.5}V_2(PO_4)_3$/C (Figure S3a,b, Supporting Information, respectively) have two kinds of morphologies, such as block-like and nanorod-like.

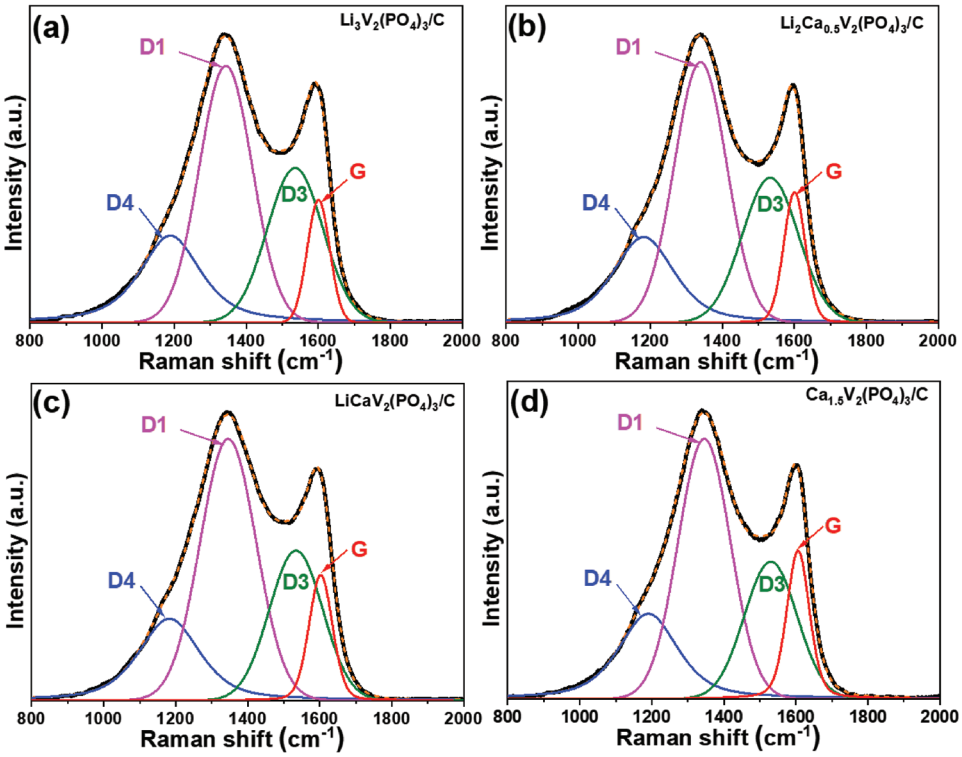

Figure 2. Deconvoluted Raman spectrum of $Li_{3-2x}Ca_xV_2(PO_4)_3/C$.

Raman scattering is a very powerful tool to study the structure and properties of carbon materials.[20] All raman spectra of the $Li_{3-2x}Ca_xV_2(PO_4)_3/C$ (**Figure 2**) display two broad peaks at around 1335 cm^{-1} (D band) and 1590 cm^{-1} (G band), which are the characteristic bands of carbonaceous materials.[3] A portion of the resulting averaged spectrum (800–2000 cm^{-1}) was deconvoluted into four component bands (labeled as D1, D3, D4, and G) (Figure 2).[20,21] D1-band is caused by the breathing mode of κ-point phonons with A_{1g} symmetry in disordered graphitic structure. While G-band arises from the E_{2g} phonon of sp^2-bonded carbon atoms in graphitic materials. D3 band shows the existence of fragments or functional groups in the amorphous phase. The I_G/I_D ratio (area ratio of G band and D band) provides useful information on the graphitization degree of carbonaceous materials. The I_G/I_D ratios are 0.20, 0.22, 0.22, and 0.26 for the LVP/C, $Li_2Ca_{0.5}V_2(PO_4)_3/C$, $LiCaV_2(PO_4)_3/C$, and $Ca_{1.5}V_2(PO_4)_3/C$, respectively. Form these values it can be concluded that the graphitization degree of the carbon in $Ca_{1.5}V_2(PO_4)_3/C$ is higher than the other three materials. It has been reported that carbon materials with graphitic structure can enhance electronic conductivity in composite.[3,22] Therefore, the existence of carbon in the materials can enhance the electronic conductivity and electrochemical performance of the $Li_{3-2x}Ca_xV_2(PO_4)_3/C$.

2.2. Electrochemical Properties

Figure 3 displays the charge–discharge profiles of $Li_{3-2x}Ca_xV_2(PO_4)_3/C$ materials at 1 C in the potential range of 3.0–0.01 V versus Li^+/Li at 25 °C. As shown in Figure 3a, four pairs of charge/discharge plateaus, centered at about 1.71/1.64 V, 1.77/1.73 V, 1.90/1.86 V, 2.02/1.94 V versus Li^+/Li, can be observed in the first cycle of $Li_3V_2(PO_4)_3/C$. These four plateaus were already reported and described as a sequence of phase transition processes.[15a] They are also present on the subsequent charge–discharge curves, indicating a reversible process. At potentials below 1.6 V, a sloping profile is recorded, indicating a solid solution behavior (i.e., single phase region). As an anode material, the LVP/C material provides initial lithiation and delithiation capacities of 644.8 and 431.3 mAh g^{-1}, respectively (**Table 1**). The initial irreversible capacity loss (213.5 mAh g^{-1}) can be attributed to the formation of the solid electrolyte interphase (SEI) film on LVP, as well as on both the amorphous carbon and acetylene black (present as conductive additive).[15a,23] In the second cycle, the lithiation and delithiation capacities are 388.2 and 418.7 mAh g^{-1}, respectively, showing a reduced irreversible capacity loss (30.6 mAh g^{-1}).

$Li_2Ca_{0.5}V_2(PO_4)_3/C$ in Figure 3b exhibits similar reversible charge and discharge plateaus as $Li_3V_2(PO_4)_3/C$ at about 1.71/1.64 V, 1.77/1.73 V, 1.90/1.86 V, 2.02/1.94 V. This material shows initial lithiation and delithiation capacities of 438.5 and 273.0 mAh g^{-1}, respectively, with an initial irreversible capacity loss of 165.5 mAh g^{-1}. However, for higher Ca substitution (i.e., $LiCaV_2(PO_4)_3/C$ and $Ca_{1.5}V_2(PO_4)_3/C$, in Figure 3c,d), the plateaus completely disappear. This behavior is characteristic of the continuous change in the oxidation state of a pseudocapacitive material during the charge–discharge process, as also observed for RuO_2,[24] a typical pseudocapacitive material. $LiCaV_2(PO_4)_3/C$ and $Ca_{1.5}V_2(PO_4)_3/C$ materials

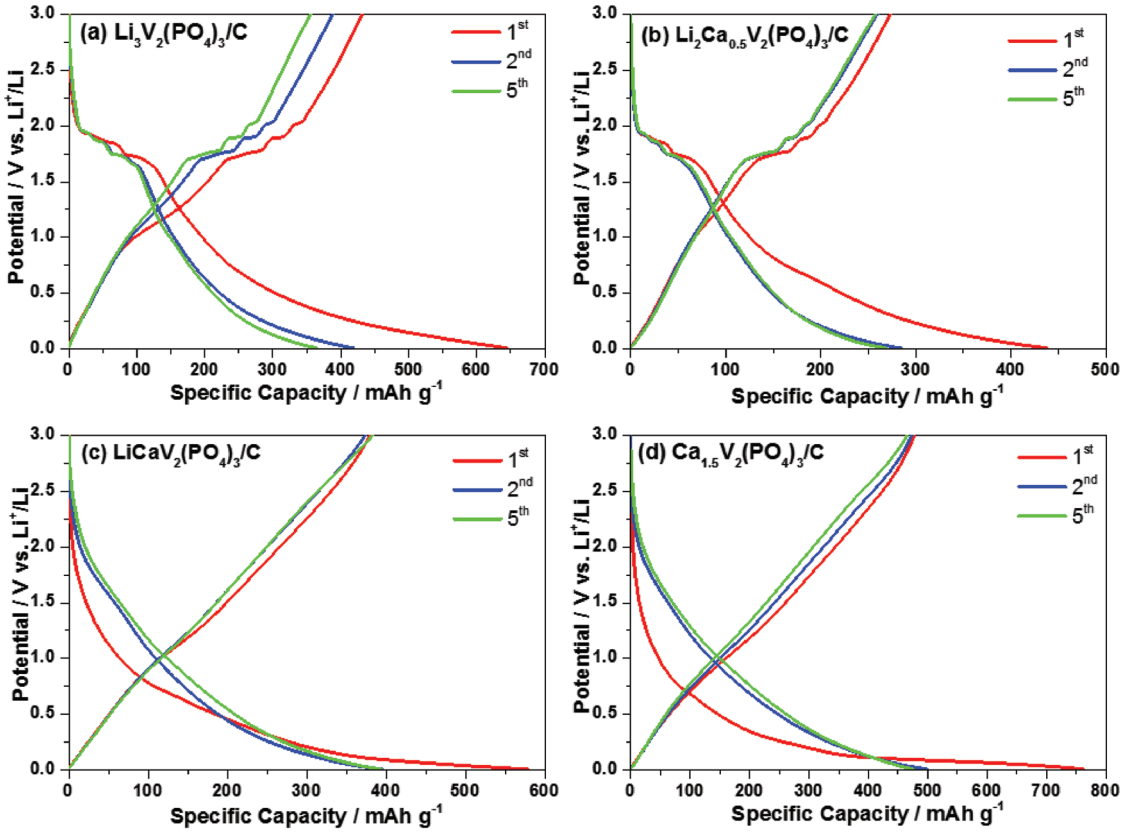

Figure 3. The charge–discharge curves of $Li_{3-2x}Ca_xV_2(PO_4)_3$/C at 1 C at 25 °C.

show an initial lithiation/delithiation capacity of 578.2/380 and 764.1/482.6 mAh g^{-1}, with an initial irreversible capacity loss of 198.2 and 281.5 mAh g^{-1}, respectively. Among the four samples, $Ca_{1.5}V_2(PO_4)_3$/C shows the highest reversible lithiation capacity of 479.7 mAh g^{-1} at the 5th cycle.

It is worth mentioning that all materials show at 1 C a much higher reversible capacity with respect to the theoretical one calculated considering 4 Li^+ ions insertion.[15a] The reason for the large excess of capacity needs to be clarified. One possible contribution to the capacity might be attributed to both the adsorption and insertion of ions (presumably with a double layer mechanism and intercalation mechanism) on/into the amorphous carbon and microsized active materials synthesized by the carbon-thermal reduction method. As demonstrated by BET, the surface area of LVP/C is 54.3 m^2 g^{-1}, while the BET surface area of $Ca_{1.5}V_2(PO_4)_3$/C is 24.8 m^2 g^{-1}. These large surface areas could contribute to the capacity during cycling. Interestingly, the theoretical capacity (calculated for the insertion of 4 Li^+) decreases along with the increasing Ca content for all compounds. The theoretical values are 262, 254, 247, and 239 mAh g^{-1} for $Li_3V_2(PO_4)_3$ $Li_2Ca_{0.5}V_2(PO_4)_3$, $LiCaV_2(PO_4)_3$, and $Ca_{1.5}V_2(PO_4)_3$, respectively. However, the experimental capacity of $Ca_{1.5}V_2(PO_4)_3$ is much higher (≈110 mAh g^{-1} more) than that of LVP.

Figure 4a provides the specific capacities delivered at increasing C-rates, ranging from 1 to 200 C. Among the four samples, $Ca_{1.5}V_2(PO_4)_3$/C material delivers the highest specific lithiation capacity until 40 C, while the $Li_2Ca_{0.5}V_2(PO_4)_3$/C shows the lowest one. At C-rates higher than 40 C, the capacities of all samples are very close to each other. As shown in Figure 4a, the specific capacities are 389.7, 273.6, 392.7, and 492.9 mAh g^{-1} at 1 C for the LVP/C, $Li_2Ca_{0.5}V_2(PO_4)_3$/C, $LiCaV_2(PO_4)_3$/C, and $Ca_{1.5}V_2(PO_4)_3$/C electrodes, respectively. At 200 C (an extremely high C-rate for battery materials), the electrodes are still able to deliver specific capacities higher than 50 mAh g^{-1}. Figure 4b shows the capacity retention of the $Li_{3-2x}Ca_xV_2(PO_4)_3$/C. The LVP/C displays outstanding capacity retention when increasing the current rate. All the substituted

Table 1. Summary of the specific capacities of $Li_{3-2x}Ca_xV_2(PO_4)_3$/C in the 1st cycle (mAh g^{-1}).

Sample	1st lithiation capacity	1st delithiation capacity	1st irreversible capacity	5th lithiation capacity	5th delithiation capacity	5th irreversible capacity
$Li_3V_2(PO_4)_3$/C	644.8	431.3	213.5	365.4	355.5	9.9
$Li_2Ca_{0.5}V_2(PO_4)_3$/C	438.5	273.0	165.5	268.9	257.9	11.0
$LiCaV_2(PO_4)_3$/C	578.2	380	198.2	393.4	383.3	10.1
$Ca_{1.5}V_2(PO_4)_3$/C	764.1	482.6	281.5	479.7	470.3	9.4

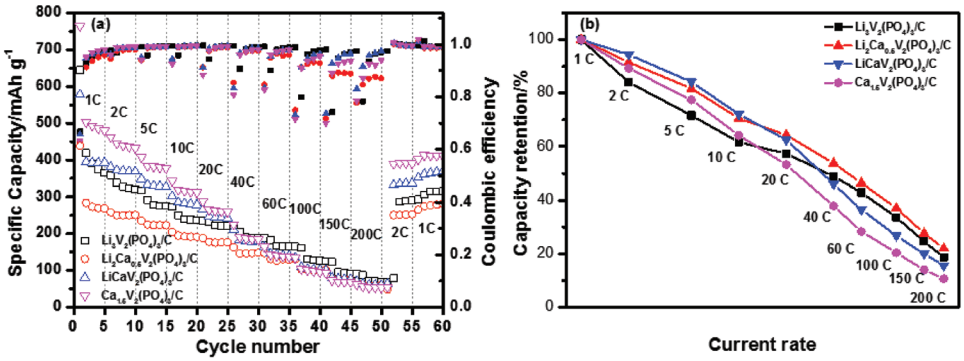

Figure 4. Specific capacities at increasing C-rates of the $Li_{3-2x}Ca_xV_2(PO_4)_3$/C electrodes.

samples demonstrate a higher capacity retention than that of LVP/C when the current rate is lower than 20 C. At 20 C, it can still have a capacity retention of 57%, 64%, 63%, and 53%, respectively, along with the increase of Ca amount. All samples display superior rate performance and this behavior can be related to three main factors: 1) the submicron sized $Li_{3-2x}Ca_xV_2(PO_4)_3$/C particles, which reduce the diffusion pathway of the Li ions; 2) and the good electronic conductivity provided by the carbon coating; 3) the substituted Ca-ion can provide more vacancies in the structure and therefore benefit to the ion transport. In particular, the Ca-substituted samples with higher amount of Ca deliver much higher capacity than the LVP/C.

2.3. Study of the Reaction Mechanisms

The working mechanism of these electrodes was studied by combining electrochemical and spectroscopic techniques. **Figure 5** displays the cyclic voltammetry of the four samples. $Li_3V_2(PO_4)_3$/C shows five clear reduction peaks at 1.95, 1.86, 1.74, 1.72, and 1.66 V between 2.0 V and 1.6 V, while on its reverse scan process, five oxidation peaks are detected at 1.72, 1.75, 1.78, 1.90, and 2.02 V. It is noteworthy to point out that previously, Zhang et al.[15b] have reported that the CV of $Li_3V_2(PO_4)_3$/C only has four clear oxidation and four reduction peaks, with a pair of vague peaks at 1.72/1.76 V. Rui et al.[15a] suggested that ≈0.5 Li^+ are inserted at every step, corresponding to the following composition changes: $Li_3V_2(PO_4)_3 \rightarrow Li_{3.5}V_2(PO_4)_3 \rightarrow Li_4V_2(PO_4)_3 \rightarrow Li_{4.5}V_2(PO_4)_3 \rightarrow Li_5V_2(PO_4)_3$. They stated that in total two Li^+ are inserted into the LVP structure between 2.0 and 1.6 V versus Li^+/Li, while below 1.6 V versus Li^+/Li an additional reversible insertion–deinsertion process takes place through a solid solution reaction, with the uptake of further two Li^+ (to form $Li_7V_2(PO_4)_3$). In contrast with all previous reports, herein, for the first time, we clearly observe five oxidation and reduction peaks between 1.6 and 2.2 V in $Li_3V_2(PO_4)_3$, suggesting a metastable phase formation. It is worthy to mention that only four pairs of plateaus can be observed in the discharge–charge profiles. This difference is due to the fact that the intensity of the redox peaks 1.75/1.72 V is too low compared with the very close redox peaks 1.78/1.74 V, therefore these two processes can be distinguished only at very low rate. The galvanostatic cycles are performed at 1 C, which is a fast discharge–charge rate. Instead, the CV was done with the very low scan rate of 0.05 mV s^{-1} which allows to separate the two processes. A broad peak near 0 V can be seen in the first cycle. This peak can be attributed to the Li ions insertion into amorphous carbon and the decomposition of the electrolyte to form a SEI film.[15b,25] In the following scans, this peak is weaker and contributes to lower capacity than that for the first cycle (Figure S4a, Supporting Information). With a low level of Li^+ substitution with Ca^{2+} ($Li_2Ca_{0.5}V_2(PO_4)_3$/C) the main 5 redox reactions, which are present on the pristine $Li_3V_2(PO_4)_3$/C are still maintained. Moreover, in the CV of $Li_2Ca_{0.5}V_2(PO_4)_3$/C two additional features are observed: one pair of broad reduction/oxidation peaks at 1.50 V/1.63 V and one irreversible oxidation at 2.24 V (Figure S4b, Supporting Information). On the other side, the other two compounds with higher Ca-content do not show any obvious redox peaks, but rather a box-type CV shape.

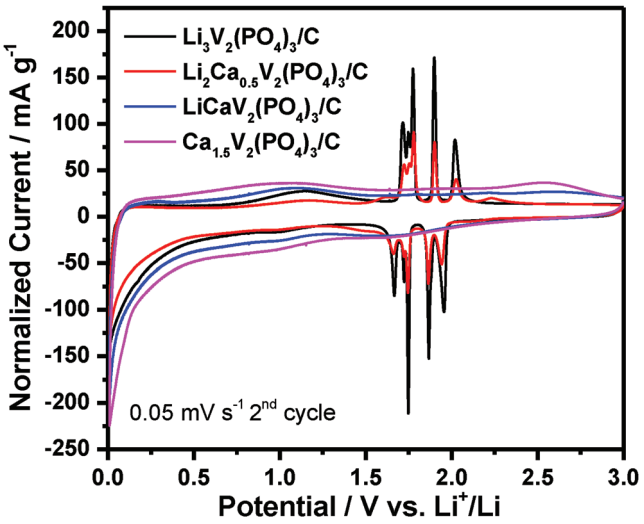

Figure 5. The 2nd CV curves of $Li_{3-2x}Ca_xV_2(PO_4)_3$/C at scan rates of 0.05 mV s^{-1}.

Cyclic voltammetry was further performed at different scan rates (from 0.05 to 2 mV s^{-1}), in order to analyze the reaction kinetics (Figure S5, Supporting Information). By increasing the

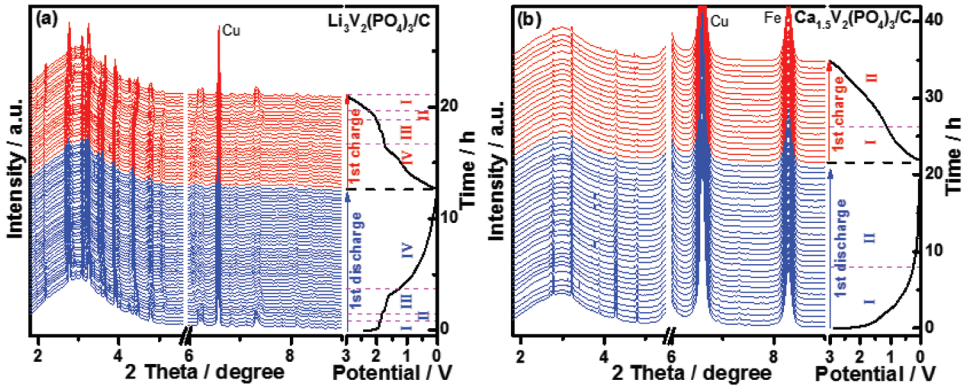

Figure 6. In operando synchrotron diffraction patterns of $Li_{3-2x}Ca_xV_2(PO_4)_3$/C for the 1st cycle with the rate of C/8.

scan rate, highly symmetrical and clearly split anodic/cathodic peaks are still exhibited (Figure S5a,b, Supporting Information).

According to Muller's work,[26] the peak current obeys a power-law relationship with the sweep rate: $i = av^b$.

Here a is a constant and v is the sweep rate. The b value can vary between 0.5 and 1.0, where a value of 0.5 indicates a diffusion controlled process and the value of 1.0 indicates a surface process (generally attributed to a capacitive-type process). The b value can be determined by the slope of log(i) versus log(v), as shown in Figure S6 (Supporting Information). For $Li_3V_2(PO_4)_3$/C, the b value related to the reduction (1.74 V) and oxidation peaks (1.78 V) are 0.67 and 0.71, respectively, indicating that the electrochemical reaction related to $Li_3V_2(PO_4)_3$/C proceeds with mixed contribution of diffusion controlled and pseudocapacitive process. For the $Li_2Ca_{0.5}V_2(PO_4)_3$/C, the b values related to the reduction and oxidation peaks at 1.75/1.78 V and at 1.0/1.2 V are 0.75/0.77 and 0.98/0.90, respectively, indicating a mixed contribution of a diffusion controlled and a pseudocapacitive process, with predominance of the pseudocapacitive one. In the case of $LiCaV_2(PO_4)_3$/C and $Ca_{1.5}V_2(PO_4)_3$/C materials, b values are 0.89/0.91 and 0.93/0.89 at 1.0/1.1 V, respectively, even closer to 1, suggesting that both samples are based on the pseudocapacitive mechanism.

In order to further clarify the reaction mechanism of $Li_{3-2x}Ca_xV_2(PO_4)_3$/C during the discharge/charge process, in operando synchrotron diffraction was performed in the potential range of 3.0–0.01 V with C/8 rate. **Figure 6** displays the two extreme cases of LVP and $Ca_{1.5}V_2(PO_4)_3$. As shown in Figure 6a, all reflections of LVP can be indexed to a monoclinic structure with a space group of $P2_1/n$. At the beginning of the 1st discharge (Li-insertion), the reflections of LVP almost keep unchanged, indicating a solid solution process occurring with the Li^+ insertion (**Region I**). Some new reflections appear at 2.74°, 3.12°, 3.27°, and 4.32° in a very short time, while other reflections (at 2.76°, 3.09°, 3.25°, 3.66°, 6.18°, and 7.32°) related to LVP decrease, suggesting a very short two-phase reaction (**Region II**). Afterward, the reflections related to the new phase shift to lower angles at 1.98°, 2.19°, 2.74°, 2.78°, 3.12°, 3.23°, 3.27°, 3.55°, 3.66°, 3.92°, 4.45°, 4.83°, and 6.24°, indicating an obvious solid solution reaction (**Region III**). In **Region IV**, all the positions of reflections keep unchanged until the end of the 1st discharge, while their intensities slightly decrease. This might be attributed to the formation of SEI on the surface of the electrode material. During the 1st charge process (Li-deinsertion), the material displays a reversible behavior. First, all positions of reflections keep unchanged (**Region IV**) and then shift to higher angles (**Region III**), followed by a very short two-phase reaction and finally a solid solution (**Region II+I**). It is worthy to note that these reflections return back to the initial position related to the pristine LVP at the end of the 1st charge, suggesting a very good reversible structural change during the electrochemical process.

The structural parameters and phases ratios are displayed in Figure S7a (Supporting Information). At the beginning of the Li-insertion, the phase LVP (LVP-phase1) in **Region I** undergoes a solid solution mechanism with almost constant a, b, and c. After that, the LVP in **Region II** goes through a short two-phase region with an LVP-phase2, which has the same space group ($P2_1/n$) as the pristine LVP but with different lattice parameters. In **Region III**, the LVP-phase2 goes through a solid solution with a two-step mechanism. In this region, a increases in a stepwise, b increases continuously, while c first decreases and then increases. Upon insertion of additional 2 Li ions (**Region IV**), the lattice parameters of LVP-phase2 (a, b, c, and β) keep constant and undergoes a very long range until the end of the discharge with a volume change of ≈3.7%. In a specular way, during the charge process, the LVP-phase2 in **Region IV** keeps unchanged until around 2 V, followed by a solid solution (**Region III**). In **Region III**, the lattice parameters of LVP-phase2 display a reversible behavior, where a decreases in two steps, b decreases continuously, and c first decreases and then slightly increases. In **Region II**, the LVP-phase2 goes through a short two-phase region with LVP-phase1. At the end of the charge process (**Region I**), the LVP-phase1 undergoes a solid solution mechanism with an increase of a, a decrease of b, and constant c. Our results give a novel inside into the understanding of the lithium storage mechanism in LVP. Indeed, in their report Zhang et al.[15b] proved via in operando XRD a two-phase reaction in the potential range 3.0–1.6 V, corresponding to about 2 Li-ions insertion, in agreement with our findings. However, in the low potential region (1.6–0.01 V), they observed a slight shift of several reflections, indicating a solid solution reaction, while we do not have evidence of phase change. This could be an indication of pseudocapacititve mechanism induced by a different size and morphology of our LVP. In the same way, Dunn and co-workers proved that a material can behave as pseudocapacitor when the particle size is going to nanoscale.[27]

By contrast, all reflections of $Ca_{1.5}V_2(PO_4)_3$/C materials only slightly shift to lower 2-theta value at 2.77° 3.22°, 3.87°, 4.29°, 4.80°, 6.92°, 7.33°, 8.74°, and 8.93°, during the 1st discharge process (**Region I**, Figure 6b). Meanwhile, the intensities of $Ca_{1.5}V_2(PO_4)_3$/C slightly decrease. In **Region II**, the position of reflections related to $Ca_{1.5}V_2(PO_4)_3$/C keep constant and their intensities continuously decrease. With the progress of Li insertion, some weak reflections at a high angle become almost invisible. The deinsertion process is completely reversible. The reflections related to $Ca_{1.5}V_2(PO_4)_3$/C first keep constant (**Region II**) and then slowly shift back to its original position (**Region I**) with a slightly increase of intensities. However, it is important to notice that the intensities related to $Ca_{1.5}V_2(PO_4)_3$/C do not return back to their original ones. Figure S7b (Supporting Information) shows that during the 1st lithiation process (**Region I**), the lattice parameter *a* increases slightly (until the potential of 0.45 V, corresponding to the uptake of 2.76 Li ions) and *c* keeps constant (near-zero volume change ≈0.34%). At potential lower than 0.45 V, the lattice parameters *a* and *c* keep constant until the end of discharge. Upon charging, the lattice parameter *a* keeps constant, followed by a decrease to its original value. The lattice parameter *c* keeps stable until 1.85 V and finally slightly decreases. The almost unchanged structure of the $Ca_{1.5}V_2(PO_4)_3$/C confirms the hypothesis of a predominance of a pseudocapacitive mechanism, as highlighted by the absence of redox peaks in the cyclic voltammetry. Moreover, as a zero-strain material, $Ca_{1.5}V_2(PO_4)_3$/C has even more potentialities with respect to the well-known $Li_4Ti_5O_{12}$,[28] delivering a lower operating potential and a higher capacity, thus enabling higher energy density.

In order to investigate the local electronic structure and environment of the active materials, in operando XAS was performed on pure LVP/C and fully substituted $Ca_{1.5}V_2(PO_4)_3$/C. The normalized V K-edge X-ray absorption near edge structure (XANES) spectra collected during the 1st lithiation are shown in **Figure 7**. In case of LVP, the graphs are grouped in three main regions (Figure 7a): i) from OCV (pristine state) to 1.77 V (corresponding to 1 Li^+ insertion), ii) from 1.77 to 0.80 V (corresponding to the consumption of additional 2 Li^+ ions), and iii) from 0.80 to 0.01 V (where additional 4.17 Li^+ ions are consumed). During the reduction process in total 7.17 moles of Li^+ are consumed. From OCV to 0.80 V, the edge position of V K-edge for LVP continuously shifts to lower energy. The pre-peak (A in Figure 7a) also shifts to lower energy and decreases in intensity, indicating

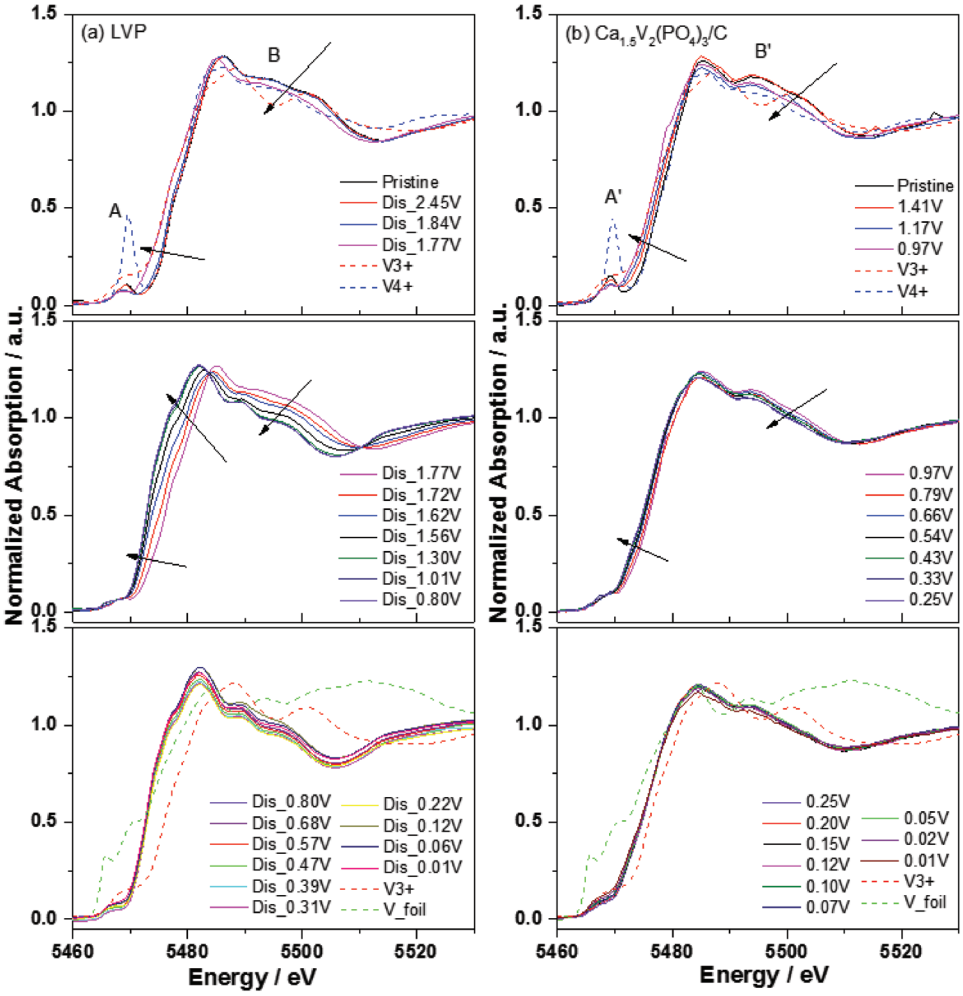

Figure 7. V K-edge XANES spectra of LVP a) and $Ca_{1.5}V_2(PO_4)_3$ b) during the 1st lithiation process.

a reduction of the average valence state of vanadium during Li-insertion. The weak preedge peak on the XANES spectra for the V K-edge of pristine LVP is attributed to the transitions between the 1s and bound p-hybridized d-states, which is very similar to the spectrum of V_2O_3.[29] The edge resonance (B in Figure 7a) shows obvious changes in both intensity and shape, which are related to the energy absorption by core electrons. The two edge resonance at energy of 5489 and 5497 eV become more resolved and their intensity decrease along with the lithiation from OCV to 0.8 V. Meanwhile, the white line is clearly separated with the edge resonance, resulting in a clear peak at 5481 eV. At the potential of 1.77 V (1 Li-insertion), the V oxidation state is reduced from V^{3+} (pristine LVP) to $V^{2.5+}$, corresponding to 1 Li ion insertion. By reducing the potential from 1.77 to 0.8 V (corresponding to the consumption of additional 2 Li ions), the edge position continuously shifts to lower energy and the pre-peak shifts to lower energy, showing a reduction of vanadium to an oxidation state of $V^{1.5+}$ according to electrochemistry data. By further decreasing the potential from 0.8 to 0.01 V (corresponding to the consumption of 4.41 Li^+), the edge position keeps almost unchanged. Unfortunately, a reference related to V^{2+} and V^+ (necessary to estimate the absolute oxidation state at 0.01 V) is, so far, not available and it is not possible to prove the oxidation state of vanadium at very low potential. However, the very slight change of the edge position cannot justify the insertion of such large amount of lithium. Part of the lithium consumed in the first cycle forms the SEI. Part of the reversible lithium inserted can be stored inside the carbonaceous material present in the electrode (carbon coating and conductive additive).

On the same way, the XAS spectra related to $Ca_{1.5}V_2(PO_4)_3$ are divided into three groups: i) OCV to 0.97 V (corresponding to 1 Li^+ insertion), ii) from 0.97 to 0.252 V (consumption of additional 2 Li ions), iii) from 0.252 to 0.01 V (consumption of 4.10 Li ions). During the lithiation process, from OCV to 0.97 V, the edge position of V K-edge for $Ca_{1.5}V_2(PO_4)_3$ continuously shifts to lower energy and the pre-peak (A′ in Figure 7b) also shifts to lower energy with the decrease of intensity, indicating a reduction in the average valence state of vanadium. At the potential of 0.97 V (1 Li ion insertion), the V oxidation state is reduced from V^{3+} (pristine $Ca_{1.5}V_2(PO_4)_3$) to $V^{2.5+}$, corresponding to 1 Li ion insertion. The edge resonance at the energies of 5494 and 5501 eV (B′ in Figure 7b) also shows a decrease of intensity along with the lithiation from OCV to 0.97 V. Differently than what observed for LVP, the edge resonance for $Ca_{1.5}V_2(PO_4)_3$ shows a very slight decrease of the intensity without the formation of three resolved peaks. From 0.25 to 0.01 V, the edge position keeps almost unchanged, displaying a similar behavior as that for LVP. The XAS results clearly show that V cannot be reduced to a lower oxidation state after the insertion of 3 Li ions, suggesting that at low potential the capacity is not due to the Li^+ insertion into the host materials, but has to be related to another mechanism, like ion adsorption with a double layer formation, insertion into amorphous carbon with disordered structure and the SEI contribution.

3. Conclusion

In this work, $Li_{3-2x}Ca_xV_2(PO_4)_3/C$ (x = 0, 0.5, 1, and 1.5) anode materials were synthesized by the carbon-thermal method. Synchrotron diffraction shows that LVP/C has a monoclinic structure with the space group of $P2_1/n$. When x is 0.5 and 1, $Li_2Ca_{0.5}V_2(PO_4)_3/C$ and $LiCaV_2(PO_4)_3/C$ can be identified as a mixture of two phases, including monoclinic $Li_3V_2(PO_4)_3/C$ with a space group of $P2_1/n$ and rhombohedral $Ca_{1.5}V_2(PO_4)_3/C$ with a space group of R-3c, respectively. SEM of the $Li_{3-2x}Ca_xV_2(PO_4)_3/C$ samples displays agglomerates with a particle size of about 100–600 nm. Here is the first time that five reduction and oxidation peaks (instead of four, as stated in previous reports) are observed in the cyclic voltammetry of LVP/C and $Li_2Ca_{0.5}V_2(PO_4)_3/C$. On the other hand, $LiCaV_2(PO_4)_3/C$ and $Ca_{1.5}V_2(PO_4)_3/C$ have no obvious oxidation and reduction peaks and their CV profile resemble to a capacitive-like behavior. Indeed, by a kinetic analysis, these two materials display a capacitive-like mechanism, which involves fast electron transfer at the surface of the electrode. $Li_{3-2x}Ca_xV_2(PO_4)_3/C$ compounds deliver specific capacities of 389.7, 273.6, 392.7, and 492.9 mAh g^{-1} at 1 C for x = 0, 0.5, 1, and 1.5, respectively. These values are much higher than the theoretical ones. In operando synchrotron diffraction demonstrates that LVP/C undergoes two solid-solution and a short two-phase reaction during lithiation and delithiation processes and $Ca_{1.5}V_2(PO_4)_3/C$ only goes through capacitive-like mechanism. In operando XAS confirms that the V is reduced during the first 3 Li-ions insertion for both LVP/C and $Ca_{1.5}V_2(PO_4)_3/C$. Among the different compositions, $Ca_{1.5}V_2(PO_4)_3/C$ displays the highest discharge capacity until 40 C. At 200 C (an extreme high C-rate for battery materials), the cell polarization sensibly increases, but the electrodes are still able to deliver specific capacities higher than 50 mAh g^{-1}. From the electrochemical performance point of view, the Ca-substituted materials are promising candidates for the realization of advanced high power and energy devices. However, it is still unclear what the deep reason behind the additional capacity is. A role could be played by the reversible SEI formation, which will be studied by XPS in the future. On the other hand, the binder could also play an important role for the additional capacity contribution.

4. Experimental Section

Synthesis of $Li_{3-2x}Ca_xV_2(PO_4)_3/C$: All the $Li_{3-2x}Ca_xV_2(PO_4)_3/C$ (x = 0, 0.5, 1.0, and 1.5) materials were synthesized by ball-milling and carbon-thermal reduction method, as described elsewhere.[30] Poly(acrylic acid) (PAA) and D-(+)-glucose act as carbon sources and reducing agents. In detail, the starting materials $Li_2CO_3/CaCO_3$, NH_4VO_3 (9.80 mmol), and $NH_4H_2PO_4$ (14.70 mmol) with a molar ratio of (Li:Ca:V:P = (3–2x):x:2:3), were added to 20 mL of ethanol together with PAA (0.29 mmol) and D-(+)-glucose (1.12 mmol). The mixture was ball-milled with 180 ZrO_2 spheres of 5 mm for 8 h at 350 rpm. Ball-milling was interrupted every 5 min and the system was let to rest for 7 min, in order to avoid the heating of the solution. The solvent was evaporated under N_2 atmosphere at 60 °C for 12 h and the remaining powder was ground for 1 h, followed by an annealing in two steps in Ar:H_2 atmosphere (5% H_2): the powder was first heated at 350 °C for 5 h with a heating rate of 5 °C min^{-1} and then was kept at 800 °C for 8 h with a heating rate of 3 °C min^{-1}. Finally, the obtained black powder was ground with mortar and pestle for 1 h.

Structural and Morphological Characterization: Structural characterization was carried out using synchrotron radiation at Petra-III beamline P02.1 at DESY in Hamburg, Germany (λ = 0.20720 Å).[31] Powder samples were measured under a glass capillary geometry (0.5 mm in diameter). The details of the in operando setup can be found

elsewhere.[32] The diffraction data were analyzed by the Rietveld method using the Fullprof software package.[33] SEM was carried out on a Zeiss Supra 55 Scanning Electron Microscope to evaluate the morphology of the particles. TGA was done on STA 449C (Netzsch GmbH) under O_2 flow to determine the carbon content in $Li_{3-2x}Ca_xV_2(PO_4)_3$/C. Raman measurement was performed on a Labram Evolution HR FROM Horiba equipped with Nd:YAG laser (633 nm, 100 mW) and a CCD detector (Horiba). Besides, a 600 grating was used to split the measurement signal. The data were collected on $A \times 100$ objective (NA 0.95) for 20 s with 1×10^{-3} W of the laser.

Specific Surface Area and Porosity: The Brunauer–Emmett–Teller method[34] was applied to determine the specific surface areas (SSA_{BET}) of $Li_{3-2x}Ca_xV_2(PO_4)_3$/C samples. The samples were heated at 573 K for 48 h and degassed at ≈368 K for 96 h before measuring the molecular adsorption on the particles. During the degassing process about 13% mass loss was recorded for all samples. Argon gas at 87.3 K was used as the adsorbate. Ar provides a better adsorption for the estimation of SSA because of its monotonicity and nonlocalization of the adsorbent during adsorption.[35] The gas sorption was performed with an Autosorb 1-MP Instrument (Quantachrome GmbH, Germany). The pore size volume distribution, but also the specific surface area, denoted as SSA_{DFT}, were calculated with models based on DFT/Monte Carlo methods assuming mixture of spherical and cylindrical pores on an carbon-based substrate.[36]

Electrochemical Characterization: The working electrode (WE) was prepared by mixing 80 wt% of active materials ($Li_{3-2x}Ca_xV_2(PO_4)_3$/C), 10 wt% of super P and 10 wt% of Na-Alginate binder in H_2O/isopropanol (ratio of 3:1). The obtained slurry was coated on a Cu-foil and dried at room temperature. The coated Cu-foil was cut into circular pieces of 12 mm diameter (1.131 cm^2), which were then pressed at 4 tons with a hydraulic press. These electrodes (≈2 mg cm^{-2}) were dried in the vacuum oven (Büchi Labortechnik GmbH) at 120 °C for at least 12 h in order to remove all water in the micropores. Then, the dried electrodes were hermetically transferred to an Ar-filled glovebox (MBRAUN GmbH). Cyclic voltammetry (CV) and galvanostatic cycling with potential limitation (GCPL), were studied in 3-electrode Swagelok T-cells between 3 and 0.01 V using metallic lithium as a counter and a reference electrode with Whatman separator and 1 M $LiPF_6$ in EC/DMC (1:1 wt%) as electrolyte (LP30, BASF). All electrochemical measurements (CV and GCPL) were done on a VMP3 multichannel potentiostat (Biologic Science Instrument) with an EC-lab software for instrument operation and data evaluation.

In Operando Synchrotron Diffraction and In Operando XAS: In operando synchrotron diffraction was performed at PETRA-III beamline P02.1 at DESY in Hamburg, Germany. The in operando cells for synchrotron diffraction were built by using 2025-type coin cells with 5 mm diameter glass windows (thickness of 0.13–0.16 mm). The working electrode materials were pressed on Cu mesh; the Li metal counter electrode was prepared with a hole of 5 mm in the center. These in operando cells were cycled with a C/8 rate during data collecting. The theoretical capacity (1 C) was considered as 266 mAh g^{-1} referring to the insertion of 4 Li^+ for LVP.[15a] In operando XAS measurements were carried out at PETRA-III beamline P65 at DESY in Hamburg during the first cycle with a C/8 rate between 3 and 0.01 V. XAS spectra were recorded in quick-XAS (8 min per spectrum) mode in fluorescence geometry using a passivated implanted planar silicon (PIPS) diode. The V K-edge of $Li_{3-2x}Ca_xV_2(PO_4)_3$/C was measured during the electrochemical cycling and the energy was calibrated using the absorption edge of V foil, as it is commonly employed in XAS experiments. All data were collected at room temperature with a Si (111) double crystal monochromator and all XAS spectra were processed using DEMETER software package.[37]

Supporting Information

Supporting Information is available from the Wiley Online Library or from the author.

Acknowledgements

This work contributed to the research performed at CELEST (Center for Electrochemical Energy Storage Ulm-Karlsruhe). The authors acknowledge the synchrotron radiation source Petra-III (DESY) in Hamburg, Germany, for provision of beam-time at the P02.1 and P65 beamline. The authors would like to thank Alexander Schoekel from Experiments Division in DESY, Hamburg. The in operando XAS work was performed by using the Biologic potentiostat of PETRAIII beamline P02.1. The authors thank the financial support of the Ministry of Science and Culture Baden Württemberg (M.W.K.) through the "Brigitte-Schlieben-Lange Programm."

Conflict of Interest

The authors declare no conflict of interest.

Keywords

Ca-substitution, in operando synchrotron diffraction, in operando X-ray absorption spectroscopy, $Li_3V_2(PO_4)_3$, Li-ion batteries

Received: June 11, 2019
Revised: July 2, 2019
Published online: July 31, 2019

[1] a) M. S. Whittingham, *Chem. Rev.* **2004**, *104*, 4271; b) D. Larcher, J. M. Tarascon, *Nat. Chem.* **2015**, *7*, 19; c) G. Jeong, Y.-U. Kim, H. Kim, Y.-J. Kim, H.-J. Sohn, *Energy Environ. Sci.* **2011**, *4*, 1986; d) V. Etacheri, R. Marom, R. Elazari, G. Salitra, D. Aurbach, *Energy Environ. Sci.* **2011**, *4*, 3243.
[2] a) B. Scrosati, J. Garche, *J. Power Sources* **2010**, *195*, 2419; b) X. Rui, Q. Yan, M. Skyllas-Kazacos, T. M. Lim, *J. Power Sources* **2014**, *258*, 19.
[3] T. Jiang, W. Pan, J. Wang, X. Bie, F. Du, Y. Wei, C. Wang, G. Chen, *Electrochim. Acta* **2010**, *55*, 3864.
[4] M. Secchiaroli, G. Giuli, B. Fuchs, R. Marassi, M. Wohlfahrt-Mehrens, S. Dsoke, *J. Mater. Chem. A* **2015**, *3*, 11807.
[5] a) J. Gaubicher, C. Wurm, G. Goward, C. Masquelier, L. Nazar, *Chem. Mater.* **2000**, *12*, 3240; b) H. Huang, S. C. Yin, T. Kerr, N. Taylor, L. F. Nazar, *Adv. Mater.* **2002**, *14*, 1525; c) M. Morcrette, J.-B. Leriche, S. Patoux, C. Wurm, C. Masquelier, *Electrochem. Solid-State Lett.* **2003**, *6*, A80.
[6] Z. Jian, W. Han, Y. Liang, Y. Lan, Z. Fang, Y.-S. Hu, Y. Yao, *J. Mater. Chem. A* **2014**, *2*, 20231.
[7] S. C. Yin, H. Grondey, P. Strobel, M. Anne, L. F. Nazar, *J. Am. Chem. Soc.* **2003**, *125*, 10402.
[8] S. C. Yin, P. S. Strobel, H. Grondey, L. F. Nazar, *Chem. Mater.* **2004**, *16*, 1456.
[9] Q. Kuang, Y. Zhao, X. An, J. Liu, Y. Dong, L. Chen, *Electrochim. Acta* **2010**, *55*, 1575.
[10] X. H. Rui, C. Li, C. H. Chen, *Electrochim. Acta* **2009**, *54*, 3374.
[11] a) Y.-z. Luo, L.-h. He, X.-h. Liu, *Trans. Nonferrous Metals Soc. China* **2015**, *25*, 2266; b) M. Ren, Z. Zhou, Y. Li, X. P. Gao, J. Yan, *J. Power Sources* **2006**, *162*, 1357.
[12] B. Wang, Y. Li, J. Zheng, M. Xu, F. Liu, W. Ao, J. Li, F. Pan, *Sci. Rep.* **2015**, *5*, 9365.
[13] W.-m. Yin, T.-t. Zhang, Q. Zhu, Q.-q. Chen, G.-c. Li, L.-z. Zhang, *Trans. Nonferrous Metals Soc. China* **2015**, *25*, 1978.
[14] C. Sun, S. Rajasekhara, Y. Dong, J. B. Goodenough, *ACS Appl. Mater. Interfaces* **2011**, *3*, 3772.

[15] a) X. H. Rui, N. Yesibolati, C. H. Chen, *J. Power Sources* **2011**, *196*, 2279; b) X. Zhang, R.-S. Kuhnel, M. Schroeder, A. Balducci, *J. Mater. Chem. A* **2014**, *2*, 17906; c) C. Wei, W. He, X. Zhang, Y. Wang, *J. Mater. Sci.: Mater. Electron.* **2016**, *27*, 11814.
[16] Z. Guo, Y. Wei, D. Zhang, X. Bie, Y. Zhang, K. Zhu, R. Zhang, G. Chen, *RSC Adv.* **2014**, *4*, 64200.
[17] a) D.-W. Wang, F. Li, M. Liu, G. Q. Lu, H.-M. Cheng, *Angew. Chem., Int. Ed.* **2008**, *47*, 373; b) A. Vu, Y. Qian, A. Stein, *Adv. Energy Mater.* **2012**, *2*, 1056.
[18] M. Castellanos, A. R. West, *J. Chem. Soc., Faraday Trans. 1* **1980**, *76*, 2159.
[19] R. Qing, M.-C. Yang, Y. S. Meng, W. Sigmund, *Electrochim. Acta* **2013**, *108*, 827.
[20] M. S. Dresselhaus, G. Dresselhaus, R. Saito, A. Jorio, *Phys. Rep.* **2005**, *409*, 47.
[21] a) A. Sadezky, H. Muckenhuber, H. Grothe, R. Niessner, U. Pöschl, *Carbon* **2005**, *43*, 1731; b) A. C. Ferrari, *Solid State Commun.* **2007**, *143*, 47.
[22] J. Wang, J. Liu, G. Yang, X. Zhang, X. Yan, X. Pan, R. Wang, *Electrochim. Acta* **2009**, *54*, 6451.
[23] a) J. Zhu, Z. Lu, S. T. Aruna, D. Aurbach, A. Gedanken, *Chem. Mater.* **2000**, *12*, 2557; b) D. Aurbach, B. Markovsky, M. D. Levi, E. Levi, A. Schechter, M. Moshkovich, Y. Cohen, *J. Power Sources* **1999**, *81–82*, 95; c) F. Yao, D. T. Pham, Y. H. Lee, *ChemSusChem* **2015**, *8*, 2284.
[24] V. Augustyn, P. Simon, B. Dunn, *Energy Environ. Sci.* **2014**, *7*, 1597.
[25] J. S. Gnanaraj, M. D. Levi, E. Levi, G. Salitra, D. Aurbach, J. E. Fischer, A. Claye, *J. Electrochem. Soc.* **2001**, *148*, A525.
[26] G. A. Muller, J. B. Cook, H.-S. Kim, S. H. Tolbert, B. Dunn, *Nano Lett.* **2015**, *15*, 1911.
[27] H.-S. Kim, J. B. Cook, S. H. Tolbert, B. Dunn, *J. Electrochem. Soc.* **2015**, *162*, A5083.
[28] T. Ohzuku, A. Ueda, N. Yamamoto, *J. Electrochem. Soc.* **1995**, *142*, 1431.
[29] J. Wong, F. W. Lytle, R. P. Messmer, D. H. Maylotte, *Phys. Rev. B* **1984**, *30*, 5596.
[30] M. Secchiaroli, F. Nobili, R. Tossici, G. Giuli, R. Marassi, *J. Power Sources* **2015**, *275*, 792.
[31] M. Herklotz, F. Scheiba, M. Hinterstein, K. Nikolowski, M. Knapp, A.-C. Dippel, L. Giebeler, J. Eckert, H. Ehrenberg, *J. Appl. Crystallogr.* **2013**, *46*, 1117.
[32] M. Herklotz, J. Weiss, E. Ahrens, M. Yavuz, L. Mereacre, N. Kiziltas-Yavuz, C. Drager, H. Ehrenberg, J. Eckert, F. Fauth, L. Giebeler, M. Knapp, *J. Appl. Crystallogr.* **2016**, *49*, 340.
[33] J. Rodríguez-Carvajal, *Newsletter* **2001**, *26*, 12.
[34] S. Brunauer, P. H. Emmett, E. Teller, *J. Am. Chem. Soc.* **1938**, *60*, 309.
[35] a) *Adsorption by Powders and Porous Solids* (Eds: F. Rouquerol, J. Rouquerol, K. Sing), Academic Press, London **1999**, p. 460; b) M. Thommes, B. Smarsly, M. Groenewolt, P. I. Ravikovitch, A. V. Neimark, *Langmuir* **2006**, *22*, 756; c) M. Thommes, K. Kaneko, V. Neimark Alexander, P. Olivier James, F. Rodriguez-Reinoso, J. Rouquerol, S. W. Sing Kenneth, *Pure and Applied Chemistry*, Vol. *87*, **2015**, p. 1051.
[36] J. Landers, G. Y. Gor, A. V. Neimark, *Colloids Surf. A* **2013**, *437*, 3.
[37] B. Ravel, M. Newville, *J. Synchrotron Radiat.* **2005**, *12*, 537.